Longitudinal In Vivo Changes in Radial Peripapillary Capillaries and Optic Nerve Head Structure in Non-Human Primates With Early Experimental Glaucoma

Gwen Musial, Suman Adhikari, Hanieh Mirhajianmoghadam, Hope M. Queener, Alexander W. Schill, Nimesh B. Patel, and Jason Porter

University of Houston, Houston, Texas, United States

Correspondence: Gwen Musial, University of Houston, 4901 Calhoun Road, Houston, TX 77204, USA; gwenmusial@gmail.com.

Received: June 24, 2021
Accepted: November 9, 2021
Published: January 7, 2022

Citation: Musial G, Adhikari S, Mirhajianmoghadam H, et al. Longitudinal in vivo changes in radial peripapillary capillaries and optic nerve head structure in non-human primates with early experimental glaucoma. *Invest Ophthalmol Vis Sci.* 2022;63(1):10. https://doi.org/10.1167/iovs.63.1.10

Purpose. There is conflicting evidence regarding whether a loss of radial peripapillary capillaries (RPCs) precedes neuronal loss in glaucoma. We examined the time course of in vivo changes in RPCs, optic nerve head (ONH) structure, and retinal nerve fiber layer thickness (RNFLT) in experimental glaucoma (EG).

Methods. Spectral domain optical coherence tomography images were acquired before and approximately every two weeks after inducing unilateral EG in nine rhesus monkeys to quantify mean anterior lamina cribrosa surface depth (ALCSD), minimum rim width (MRW), and RNFLT. Perfused RPC density was measured from adaptive optics scanning laser ophthalmoscope images acquired on the temporal half of the ONH. The time of first significant change was quantified as when values fell and remained outside of the 95% confidence interval established from control eyes.

Results. Mean ALCSD and/or MRW were the first parameters to change in eight EG eyes. RPC density changed first in the ninth. At their first points of change, mean ALCSD posteriorly deformed by 100.2 ± 101.2 µm, MRW thinned by 82.3 ± 65.9 µm, RNFLT decreased by 25 ± 14 µm, and RPC density decreased by 4.5 ± 2.1%. RPC density decreased before RNFL thinning in 5 EG eyes. RNFLT decreased before RPC density decreased in two EG eyes, whereas two EG eyes had simultaneous changes.

Conclusions. In most EG eyes, RPC density decreased before (or simultaneous with) a change in RNFLT, suggesting that vascular factors may play a role in axonal loss in some eyes in early glaucoma.

Keywords: glaucoma, radial peripapillary capillaries, adaptive optics scanning laser ophthalmoscope

Glaucoma is a group of eye diseases that are characterized by axonal loss and progressive retinal ganglion cell death and can ultimately result in irreversible vision loss.[1] Vascular-related factors have been shown to be associated with glaucoma, including lower diastolic perfusion pressure,[2–4] migraines,[5,6] nailfold capillary abnormalities,[7] smoking,[4,8] hypotension,[9,10] and sleep apnea.[11,12] Although vasculature has been considered an independent risk factor, vascular susceptibility to alterations in the translaminar pressure gradient are proposed to result in perfusion instabilities in capillaries within the lamina cribrosa and inner retinal tissues surrounding the optic nerve head (ONH).[13] This imbalance gives rise to alterations in ocular blood flow and a reduced blood supply to ONH, laminar, and radial peripallary capillaries,[14–16] potentially contributing to the pathogenesis of glaucoma.

The structural properties of the radial peripapillary capillaries (RPCs) may make them uniquely susceptible to damage resulting from elevated IOP in glaucoma. RPCs form the most superficial capillary bed in the retina and are potentially more fragile than other retinal capillaries, because they lack smooth muscle actin ensheathment, run in long parallel networks in the retinal nerve fiber layer (RNFL), and anastomose less frequently than other retinal capillaries.[14,15,17] Consequently, RPCs possess less collateral blood supply and have fewer connections to adapt to necessary changes in autoregulation in glaucoma.

There is conflicting evidence regarding whether RPCs play a role in retinal ganglion cell axon degeneration in glaucoma. Early work by Daicker et al.[18] in donor eyes with chronic glaucoma and different optic nerve atrophies found no correlation between the distribution of atrophic RPCs and associated visual field defects. Subsequent histological work showed RPCs to be lost at the same rate as RNFL axons in experimental glaucoma[19] and not to be significantly altered in their numbers in donor glaucomatous human eyes relative to normal eyes.[20] However, the former of these two studies primarily evaluated the capillary volume within the ONH and not the RNFL. Conversely, other studies have reported significant losses of RPCs in experimental glaucoma[21] and in donor eyes of glaucoma patients.[22] More recent reports examining the RPC network in vivo using optical coherence

tomography angiography (OCTA) found decreased peripapillary vessel density in glaucomatous eyes compared to age-matched controls[23–26] and decreased peripapillary vessel density in the eyes of primary open-angle glaucoma patients with visual field defects.[27] More recent work by Moghimi et al.[28] found a weak tendency for eyes with lower baseline values of vessel perfusion density to have faster rates of RNFL thickness loss in mild to moderate glaucoma over a two-year period. In addition, studies have reported correlations between vessel density loss and visual field loss in the superotemporal and inferotemporal sectors around the ONH and in visual field maps.[25,26,29] However, the general lack of in vivo data characterizing longitudinal changes in RPCs and retinal ganglion cell axons from a healthy state to early glaucoma has limited understanding of the relative time course for when changes occur, as well as how differences in RPC, RNFL, and ONH geometries relate to disease progression in living eyes.

The primary purpose of this study was to determine whether changes in RPC perfusion occur before a loss of circumpapillary RNFL thickness in early experimental glaucoma. Longitudinal changes in RPC perfusion, ONH structure, and RNFL thickness were assessed using split detector adaptive optics[30,31] and spectral domain optical coherence tomography imaging in living eyes of non-human primates with pressure-induced experimental glaucoma. Through the use of sensitive in vivo imaging techniques, this study describes the sequence of early changes in capillary perfusion, ONH structure, and circumpapillary RNFL thickness in experimental glaucoma.

Methods

All animal care experimental procedures were approved by the University of Houston's Institutional Animal Care and Use Committee and adhered to ARVO's Statement for the Use of Animals in Ophthalmic and Vision Research. Nine adult rhesus macaques (mean age = 6.6 ± 1.2 years) were used in this study. Before experimental glaucoma (EG) was induced, all animals underwent imaging (as described below) in two to four baseline sessions with the exception of one (OHT 86) in which only one baseline session was performed. The trabecular meshwork of the right eye was scarred using a clinical 532 nm laser (Zeiss Visulas 532; Carl Zeiss Meditec, Jena, Germany) to chronically elevate the intraocular pressure of each monkey's right eye (i.e., the experimental glaucoma eye), whereas the fellow eye served as a control.[32] During these laser sessions, monkeys were anesthetized with ketamine (20–30 mg/kg) and xylazine (0.8–0.9 mg/kg). Multiple laser sessions, minimally separated by two weeks, were used to slowly build up and create sustained elevated pressure. The first session involved lasering 180° of the trabecular meshwork, and each subsequent session was limited to 90°.

Following the first laser session, animals were imaged approximately every two weeks throughout the duration of the experiment. Monkeys were anesthetized with 20 to 25 mg/kg ketamine and 0.8 to 0.9 mg/kg xylazine and treated with a subcutaneous injection of atropine sulfate (0.04 mg/kg).[33] Each monkey's pupils were dilated with 2.5% phenylephrine and 1% tropicamide. A pharmacological agent (Iopidine; Alcon Laboratories, Inc., Fort Worth, TX, USA; or Combigan; Allergan, Inc., Irvine, CA, USA) was used at the start of each imaging experiment to reduce the animal's IOP and best ensure that the values of parameters measured during the experiment were the result of chronic changes due to sustained elevation in IOP. IOP was measured using an applanation tonometer (Tono-Pen XL Applanation Tonometer; Reichert Technologies, Inc., Buffalo, NY, USA).

Biometric Scaling

Biometric measurements of axial length, anterior chamber depth, lens thickness, and anterior corneal curvature were acquired from right and left eyes of each animal (LenStar; Haag-Streit, Köniz, Switzerland). These biometric parameters were used to convert field sizes in adaptive optics scanning laser ophthalmoscope (AOSLO) images from visual angle (in degrees) to physical retinal size (in micrometers). Conversions were performed by incorporating the measured biometry data into a four-surface model eye.[34,35]

Spectral Domain Optical Coherence Tomography Imaging

Scanning laser ophthalmoscope (SLO) fundus images and spectral domain optical coherence tomography (SDOCT) images of the ONH (15° or 30° field sizes) were acquired for each subject using the Heidelberg Spectralis HRA+OCT (Heidelberg Engineering, Heidelberg, Germany). These images assisted in navigating throughout the retina and optic nerve head (ONH) during AOSLO imaging sessions, as the AOSLO imaging field was small (approximately 2°). Monkey eyelids were held open using a lid speculum. Imaging was performed while monkeys wore a rigid gas permeable contact lens, which was used to prevent corneal dehydration and correct for any inherent spherical refractive errors.[34] Control eyes were imaged before imaging the EG eye in each animal.

At baseline, SDOCT scans centered on the ONH were acquired to ensure good ocular health, and all subsequent scans were acquired using the instrument's follow-up mode. Cross-sectional radial scans (20°, 48 b-scans, high-resolution, 20 frame averaging) centered on the ONH were acquired with enhanced depth imaging in all eyes. The inner limiting membrane (ILM) was automatically segmented in each b-scan using the SDOCT instrument's software, and any inaccuracies were manually corrected. Radial scans were exported from the SDOCT instrument and analyzed using programs written in MATLAB (MATLAB; The MathWorks, Inc., Natick, MA, USA). The points of the retinal pigment epithelium/Bruch's membrane interface and anterior lamina cribrosa surface (ALCS) were manually marked in as many b-scans as possible.[35] These delineated landmarks were used to calculate three ONH parameters. Bruch's Membrane Opening (BMO) was calculated as the area enclosed by an ellipse best-fit to the marked BMO points in all radial scans. Mean anterior lamina cribrosa surface depth (ALCSD) was computed as the mean distance between a plane best-fit to the marked BMO points and a thin-plate spline surface that was fit to the marked ALCS points.[36] Finally, mean minimum rim width (MRW) was computed as the mean of the minimum distances between the marked BMO points and the ILM surface across all b-scans.[37,38]

RNFL thickness was measured from 12° circular scans centered on the ONH. The raw data were analyzed using a program written in MATLAB to determine the average RNFL thickness across the entire scan and average thickness in

Investigative Ophthalmology & Visual Science

60° sectors (as later described). The thickness of the RNFL was calculated as the distance between the automatically segmented ILM (after manual correction) and the manually marked, posterior boundary of the RNFL.[39]

AOSLO Imaging

High-resolution, in vivo measurements of RPC perfusion have been carried out in healthy and glaucomatous eyes primarily using OCTA and AOSLO imaging. Although OCTA has emerged as a powerful tool to image perfused vasculature (such as RPCs) at different retinal depths over a wide field,[24,40] the presence of uncorrected ocular aberrations in the subject being examined degrades the lateral resolution of the acquired image and limits the ability to visualize the smallest perfused retinal capillaries. Therefore, we used an AOSLO to correct the eye's aberrations and provide high-resolution (~2.5 µm) in vivo images of the finest capillary structures in the retina.

AOSLO images of perfused RPCs were acquired at baseline and in subsequent imaging sessions following the initial laser session. Each monkey's head was positioned using a head mount attached to a 3-dimensional translation stage and was steered using the tip, tilt, and rotation capabilities of the head mount until the monkey's ONH was within the AOSLO's field of view. Through-focus AOSLO images were taken to determine the plane of best focus of the most superficial retinal vascular network (i.e., the RPCs in healthy eyes). En face reflectance videos of RNFL axon bundles were acquired using a confocal AOSLO imaging channel over a 2° field of view at a rate of 25 Hz using a superluminescent diode light source (S-Series Broadlighter; Superlum, Carrigtwohill, Ireland) with a center wavelength of 840 nm (FWHM = 50 nm). The power of the superluminescent diode at the corneal plane was 150 µW, a value that was more than 10 times below the maximum permissible exposure for an imaging duration of one hour.[41] Non-confocal, split detector adaptive optics videos[42] were collected simultaneously with confocal videos at the same retinal location and depth and were subsequently used to generate perfusion images.[43] The 30° SLO image acquired with the Heidelberg Spectralis HRA+OCT served as a guide for navigating to the region of retina that was imaged with the AOSLO system. In each session, images of the RPC network were acquired in the temporal hemifield around the ONH using the AOSLO system and were manually stitched together to form a montage of perfused vasculature. Images were first acquired in each animal's EG eye before proceeding to image the contralateral control eye.

SLO images from all timepoints were aligned in ImageJ (developed by Wayne Rasband, National Institutes of Health, Bethesda, MD; available at http://rsb.info.nih.gov/ij/index.html) for each subject using the plugin, StackReg, and were subsequently scaled based on each eye's ocular biometry. Small modifications in image scale were made, if necessary, to match the scale of the RPC perfusion montage acquired with the AOSLO at the baseline timepoint. Then, all subsequent RPC AOSLO montages were aligned to their corresponding SLO image taken at the same timepoint. RPC montages were then segmented with a convolutional neural network (CNN) that has been previously described.[44] Briefly, this CNN was based on a u-net segmentation structure and was trained using split detector AOSLO capillary perfusion images acquired around the ONH in both healthy human and non-human primate (NHP) eyes, and in NHP eyes with experimental glaucoma. After passing through the 20-layer CNN architecture, capillaries within the perfusion images were converted to a binary format using Otsu's method before final segmentation.[45] The CNN was trained to separately classify capillaries and larger vasculature (greater than 20 pixels in diameter).[45] Given that the primary purpose of this work was to examine changes in the RPCs during experimental glaucoma, only the capillary perfusion maps were analyzed in this study and used to calculate RPC perfusion density. The software with sample data are available on GitHub (https://github.com/porter-lab-software/AOVesselCNN).

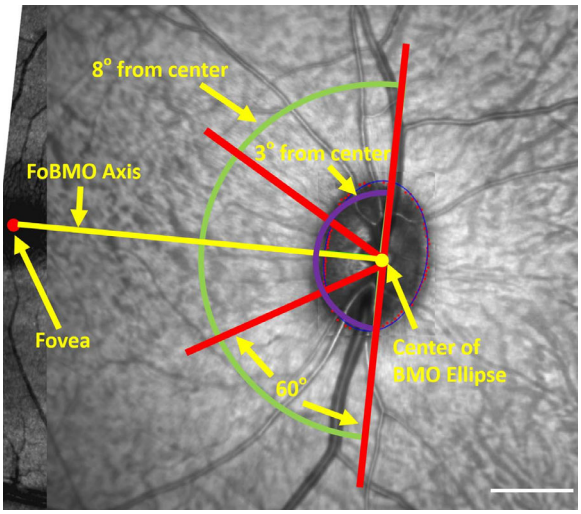

Figure 1. Use of the Fovea to Bruch's Membrane Opening (FoBMO) axis for creating 60° sectors around the optic nerve head. An ellipse (*thin blue line*) was best fit to the manually marked BMO points (*small red dots*) and used to determine the center of the BMO (*yellow dot*). The foveal center was manually marked on the SLO image (*large red dot*) and connected to the center of the BMO ellipse to form the FoBMO axis (*yellow line*). 60° sectors (corresponding to the angular subtense between red radial lines) were used in combination with annuli extended radially from 3° from the center of the BMO ellipse (*innermost purple arc*) to 8° from the center of the BMO ellipse (*outermost green arc*) for RPC analysis regions. *Scale bar*: 1000 µm

Sector Analyses

A 30° SLO image centered on the fovea was manually aligned with a 30° SLO image centered on the ONH (Adobe Photoshop; Adobe Systems, San Jose, CA). After manually marking the fovea, the fovea to Bruch's membrane opening (FoBMO) axis[46] was generated using a custom program written in MATLAB by connecting the manually marked foveal center with the center of the ellipse that was best-fit to the already marked BMO points (Fig. 1). The FoBMO axis served as the reference for generating 60° sectors around the ONH. In addition, circles were constructed at radial distances of 3° and 8° from the center of the BMO ellipse to form a 5° annulus over which RPC perfusion and RNFL parameters were analyzed.

RPC perfusion density was calculated from the binary CNN segmentations as the percentage of pixels that contained perfused capillaries relative to the total area that was imaged. This analysis was performed globally and within individual sectors defined using the FoBMO axis (Fig. 1). For global and sectoral measurements, density was

only computed if the area imaged exceeded 30% of the total area examined within the temporal hemifield annulus (i.e., the combination of the superotemporal, temporal, and inferotemporal sectors) or within a given sector, respectively. (A 30% threshold was selected based on a trade-off between the amount of coverage we could consistently achieve in all sectors across all imaging timepoints and the number of timepoints that this threshold allowed us to quantify RPC perfusion density for each sector.) Hemifield (or global) RPC density was calculated using a mask that covered the superotemporal, temporal, and inferotemporal 60° sectors to form a 180° hemifield. The mask was generated as the union of this temporal hemifield and the area imaged with the AOSLO. When analyzing a given sector from a particular imaging session, a mask was made that was the union of the given sector and the area imaged using the AOSLO. For global and sectoral measurements, the generated mask was applied to the binary CNN segmentation and the percentage of pixels containing segmented capillaries in the region covered by the mask was used to quantify RPC perfusion density.

Statistical Analysis

For SDOCT-derived parameters, the coefficients of repeatability ($1.96 \times SD \times \sqrt{2}$) were calculated for mean ALCSD, mean MRW, and RNFL thickness across repeated measures in each control eye. For each of these parameters, a 95% confidence interval was calculated for each control eye. For each contralateral EG eye, the first timepoint of significant change in each SDOCT-derived parameter was determined as the first timepoint whose value fell outside the respective 95% confidence interval and remained so at all subsequent timepoints.

Because it was not possible to safely image and obtain RPC data in all sectors within each control eye at all timepoints (due to experimental constraints), we calculated coefficients of repeatability for global and sectoral values of RPC perfusion density for each EG eye using baseline measurements (two to four measurements) and for each fellow control eye (two to five measurements). A pooled 95% confidence interval for each retinal sector was then calculated to determine the first significant timepoint of change in RPC density. As with the SDOCT-derived parameters, the first timepoints of significant change in hemifield and sectoral measures of RPC perfusion parameters and RNFL thickness for each experimental glaucoma (EG) eye were determined as the first timepoint whose value fell outside the pooled 95% confidence interval and had no subsequent timepoints with a value that fell back within the confidence interval. RPC perfusion density and RNFL thickness were also compared over the hemifield and within each sector (superotemporally, temporally, inferotemporally).

Results

Animal characteristics and IOP data for all control and EG eyes throughout the duration of the experiment are summarized in Table 1. Mean values of IOP (±SD) were 14.4 ± 2.2 mm Hg in control eyes (across all timepoints) and 28.3 ± 5.3 mm Hg in EG eyes (across all timepoints after the initial laser session, but before pharmacological intervention for imaging purposes). The maximum IOPs measured across the control eyes and the EG eyes had mean values of 18.8 ± 2.4 mm Hg and 43.4 ± 10.5 mm Hg, respectively. Mean IOP at the time of imaging was 9.2 ± 3.7 mm Hg (range, 5.4 – 15.5 mm Hg). The mean experiment duration, defined as the time between the first laser session and last AOSLO imaging session for each NHP, was 215 ± 114 days.

A summary of RNFL thickness (RNFLT), mean ALCSD, and mean MRW values in the control eyes of each animal over the experiment duration are presented in Supplementary Table S1. These data were used to calculate the coefficients of repeatability, as previously described, for determining the first points of change in the same parameters in the fellow EG eye. The mean (±SD) values for global RNFLT, mean ALCSD, and mean MRW across all control eyes were 116.4 ± 6.8 µm, 200.7 ± 24.3 µm, and 340.0 ± 50.7 µm, respectively. Coefficients of repeatability were small for all three of the OCT-derived parameters. The average coefficients of repeatability for global RNFLT, mean ALCSD, and mean MRW across animals were 6.1 ± 1.6 µm, 20.8 ± 6.4 µm, and 16.9 ± 5.9 µm respectively.

Longitudinal changes in SDOCT-derived parameters were observed in all EG eyes (Fig. 2). Global RNFLT and mean MRW decreased throughout the duration of the experiment in all NHPs (Figs. 2a, 2b). On average, across all EG eyes, the minimum values for RNFLT and mean MRW were 84.8 ± 18.2 µm and 177.8 ± 74.6 µm, respectively. These values represent a 29.7% ± 15.9% and 48.1% ± 23.4% decrease from baseline values of RNFLT and mean MRW, respectively, across EG eyes. The anterior surface of the lamina cribrosa posteriorly deformed within each EG eye over the experiment, resulting in increased values of mean ALCSD (Fig. 2c). On average, across all EG eyes, the maximum value for mean ALCSD was 420.7 ± 103.2 µm, representing a mean increase of 118.6% ± 45.0% from baseline mean ALCSD levels.

Table 1. Demographic and IOP Data for all Control and Experimental Glaucoma (EG) Eyes

			Mean IOP ± SD (mm Hg)		Maximum IOP (mm Hg)		
Animal ID	Age (yrs)	Sex	Control Eye	EG Eye	Control Eye	EG Eye	Experiment Duration (Days)
OHT 78	5.7	M	12.1 ± 2.1	23.2 ± 7.9	19	36	378
OHT 79	5.5	M	18.2 ± 1.6	34.9 ± 9.1	22	54	350
OHT 80	5.3	M	13.5 ± 2.6	29.9 ± 14.9	18	64	384
OHT 81	6.1	F	16.9 ± 2.2	25.1 ± 8.5	20	38	154
OHT 82	6.1	F	12.9 ± 1.0	34.7 ± 7.7	15	43	182
OHT 83	7.5	F	11.1 ± 1.8	21.9 ± 9.1	15	34	81
OHT 84	7.6	M	15.2 ± 3.6	38.2 ± 15.5	22	54	137
OHT 86	7.9	M	15.5 ± 2.3	20.6 ± 5.7	18	34	119
OHT 87	8.9	F	14.8 ± 2.7	26.9 ± 7.8	20	34	147
Mean ± SD	6.6 ± 1.2		14.4 ± 2.2	28.3 ± 5.3	18.8 ± 2.4	43.4 ± 10.5	215 ± 114

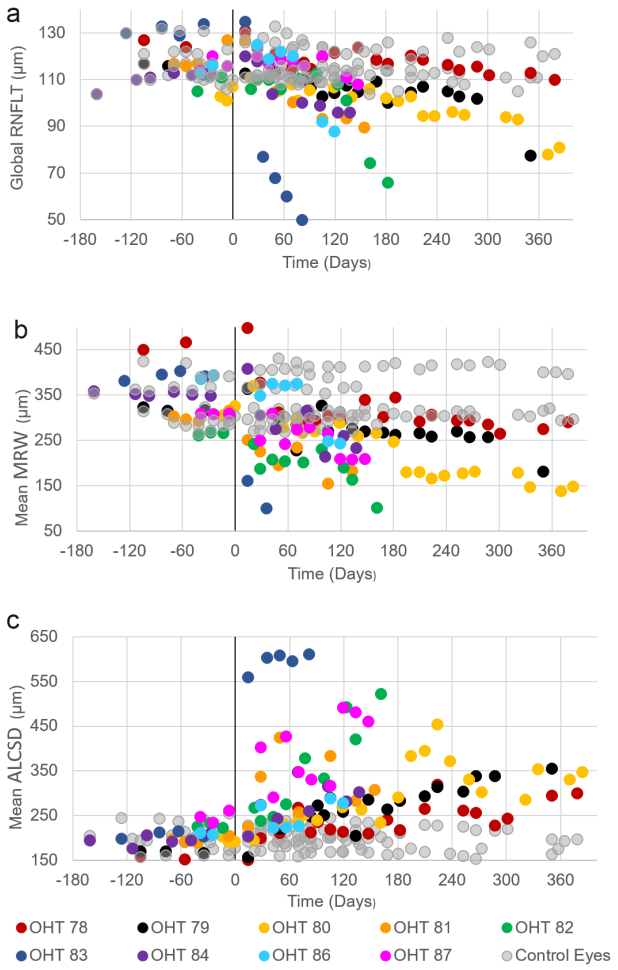

Figure 2. SDOCT-derived metrics of RNFLT, mean MRW, and mean ALCSD in all eyes as a function of time relative to the time of the first laser session (*vertical black line* at time = 0 Days) in EG eyes (*filled colored circles* with the legend at the bottom of the figure). Negative timepoints correspond to baseline measurements (before the first laser session). Control eye data are presented as *gray filled circles*. After the induction of EG, (**a**) global RNFLT decreased, (**b**) mean MRW thinned (decreased), and (**c**) the anterior laminar surface moved posteriorly, resulting in increased values of mean ALCSD over the course of the experiment.

Montages of perfused retinal vasculature acquired using AOSLO imaging in a representative control eye over the duration of the experiment are shown in Figure 3. Mean RPC perfusion density calculated across all sectors in all healthy eyes (i.e., all control eyes and all baseline measures in EG eyes) was 13.15% ± 2.97%. Mean coefficients of repeatability for perfused RPC density measured globally and in the superotemporal, temporal, and inferotemporal sectors were 3.1% ± 1.5%, 2.3% ± 1.5%, 3.6% ± 2.3%, and 4.1% ± 2.8%, respectively. Table 2 shows the baseline values of RPC density (mean ± SD) and the RPC density at the timepoint of first statistically significant change for each animal.

Longitudinal RPC perfusion images and plots of all measured parameters (Mean MRW, Mean ALCSD, global and sectoral RNFLT, global and sectoral RPC Density) are shown in Figures 4 to 6 for animals demonstrating different patterns of loss in RPC perfusion density and RNFLT. Figure 4 shows data from one representative animal (out of five) who demonstrated a decrease in RPC perfusion density prior to a thinning of the RNFL in its EG eye. In this animal, the initial loss of perfusion density in the inferotemporal sector (Figs. 4b, 4e, 4j) occurred at day 14 and persisted for the remainder of the experiment. An initial decrease in RNFLT in the corresponding inferotemporal sector was not measured until the next imaging session at day 28 (Fig. 4i).

Figure 5 shows data from one representative animal (out of two) who demonstrated an initial thinning in RNFLT before an initial decrease in RPC perfusion density. Mean ALCSD was the first parameter to initially change at 49 days after the first laser session in the EG eye of OHT-79 (Fig. 5g). At 105 days after the initial laser session, there was an initial decrease in mean MRW that was accompanied by decreases in global RNFLT and the inferotemporal sector measurement of RNFLT (Fig. 5i), as well as measurements of RPC perfusion density made globally and in the superotemporal and temporal sectors (Fig. 5j). However, the measurements of global RNFLT, global RPC perfusion density, and superotemporal and temporal RPC perfusion densities all returned to being within their respective confidence intervals at later timepoints. The first timepoint in which RPC perfusion decreased and remained outside the confidence interval occurred in the superotemporal sector at 266 days after the first laser session (Figs. 5c, 5f, 5j).

Figure 6 depicts one representative case (out of two) where initial changes in RNFLT and RPC perfusion density occurred at the same imaging timepoint. Nearly 100 days after the first changes were measured in mean MRW (day 21) and mean ALCSD (day 42), an initial thinning in global RNFLT and the inferotemporal sector measurement of RNFLT occurred on day 133 (Fig. 6g). At the same timepoint, a decrease in RPC perfusion density was measured globally and sectorally (Fig. 6h).

The first timepoints of change in all ONH and RPC parameters on global or sectoral levels are illustrated in Figure 7 for each EG eye as a function of study time relative to the date of the first laser session. An increase in mean ALCSD was among the first structural changes in seven of nine eyes. A simultaneous decrease in mean MRW occurred in six of these seven eyes, and two also exhibited a decrease in RPC perfusion density. Mean MRW was the first parameter to solely change in one EG eye (OHT 82) whereas RPC density solely changed first in the ninth EG eye (OHT 86). All EG eyes experienced decreases in RPC perfusion density and RNFLT throughout the duration of the experiment. A decrease in RPC perfusion density first occurred before the first instance of RNFL thinning in five of nine EG eyes (OHT-78, 80, 81, 83, 86). The first decrease in RPC perfusion density and RNFLT occurred simultaneously in two EG eyes (OHT-82, 87), whereas an initial thinning of the RNFL occurred before an initial decrease in RPC perfusion density in two EG eyes (OHT-79, 84).

Discussion

The purposes of this study were to (1) determine whether changes in RPC perfusion occur before changes in RNFL thickness in early experimental glaucoma and (2) characterize the time course of in vivo changes in RPC perfusion concurrent with changes in ONH structure and RNFL thickness. RPC density significantly decreased before RNFL thinning occurred in the majority of eyes studied. ONH parameters (mean ALCSD, mean MRW) changed before retinal parameters (RPC density, RNFLT) in all eyes but

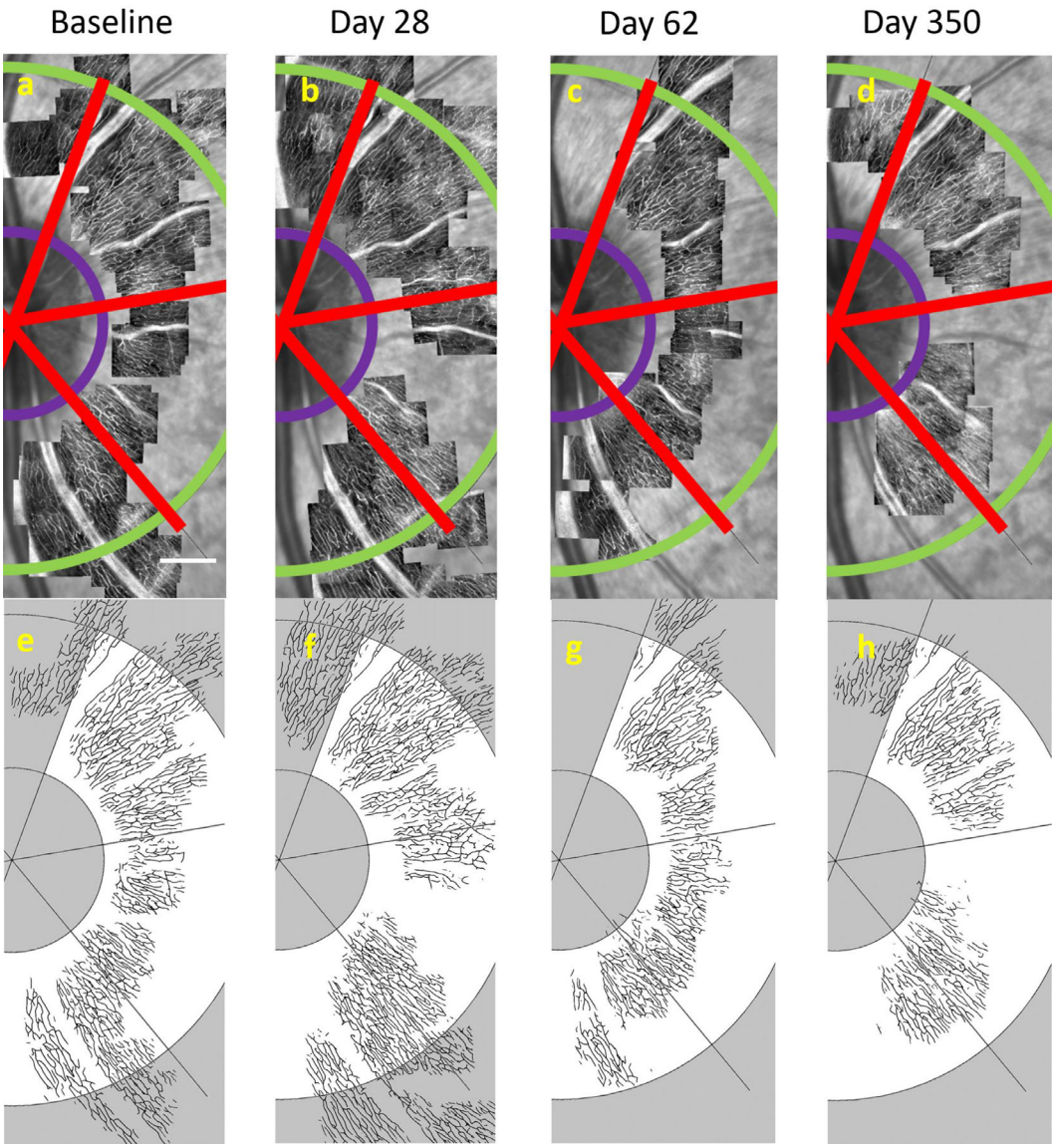

Figure 3. Perfused RPCs were consistently imaged in control eyes throughout the experiment. **(a–d)** AOSLO perfusion montages and **(e-h)** corresponding neural network segmentations from a representative control eye (OHT-78, OS) acquired at different timepoints relative to the first laser session in the contralateral EG eye. **(a)** The baseline RPC perfusion montage was overlaid on the corresponding SLO image. *Red lines* depict 60° sectoral boundaries for RPC analysis regions, as previously described in Figure 1. Perfused RPC density was analyzed in the annulus between the *inner purple arc* and *outer green arc*, located at radii of 3° and 8° from the center of the BMO ellipse, respectively. The corresponding CNN segmentation of the perfused RPCs illustrated in **a** is shown immediately below in **e**. RPC perfusion montages acquired in the same control eye and their corresponding CNN segmentations are shown at **(a, e)** baseline (IOP = 9 mm Hg), **(b, f)** 28 days (IOP = 10 mm Hg), **(c, g)** 62 days (IOP = 12 mm Hg), and **(d, h)** nearly one year (IOP = 9 mm Hg) following the initial laser session performed in the EG eye. *Scale bar*: 400 µm.

Table 2. Mean Values (±1 SD) of Hemifield (Global) and Sectoral RPC Densities at Baseline and Absolute Values at the Timepoint of First Significant Change in EG Eyes

	Global RPC Density (%)		Superotemporal RPC Density (%)		Temporal RPC Density (%)		Inferotemporal RPC Density (%)	
Animal ID	Mean ± SD	Value at First Change	Mean ± SD	Value at First Change	Mean ± SD	Value at First Change	Mean ± SD	Value at First Change
OHT 78	16.35 ± 0.95	9.68	17.49 ± 0.96	13.57	17.01 ± 1.85	5.56	16.08 ± 0.26	6.38
OHT 79	15.95 ± 1.44	9.92	16.22 ± 1.80	11.56	16.02 ± 1.26	10.08	15.34 ± 1.54	9.64
OHT 80	16.68 ± 0.93	12.36	16.18 ± 0.99	13.00	17.10 ± 1.16	13.56	16.52 ± 2.56	11.35
OHT 81	11.65 ± 0.64	7.41	13.77 ± 0.32	11.19	9.10 ± 1.48	—	11.52 ± 0.20	5.14
OHT 82	12.69 ± 0.16	7.07	12.59 ± 0.31	6.77	12.57 ± 0.24	7.47	12.86 ± 0.14	2.18
OHT 83	9.61 ± 0.66	4.32	8.75 ± 0.99	5.28	8.53 ± 0.46	5.67	11.89 ± 0.11	4.63
OHT 84	9.16 ± 0.79	—	9.57 ± 1.45	—	8.11 ± 0.43	—	9.33 ± 0.79	—
OHT 86*	13.46	7.11	13.25	6.52	12.73	—	14.23	8.37
OHT 87	11.21 ± 1.41	5.12	13.05 ± 0.23	7.60	8.87 ± 2.46	4.07	11.63 ± 2.41	3.56
Mean ± SD	12.97 ± 2.68	7.87 ± 2.48	13.43 ± 2.78	9.44 ± 3.03	12.23 ± 3.54	7.74 ± 3.21	13.26 ± 2.28	6.41 ± 2.95

* Only one baseline measurement.

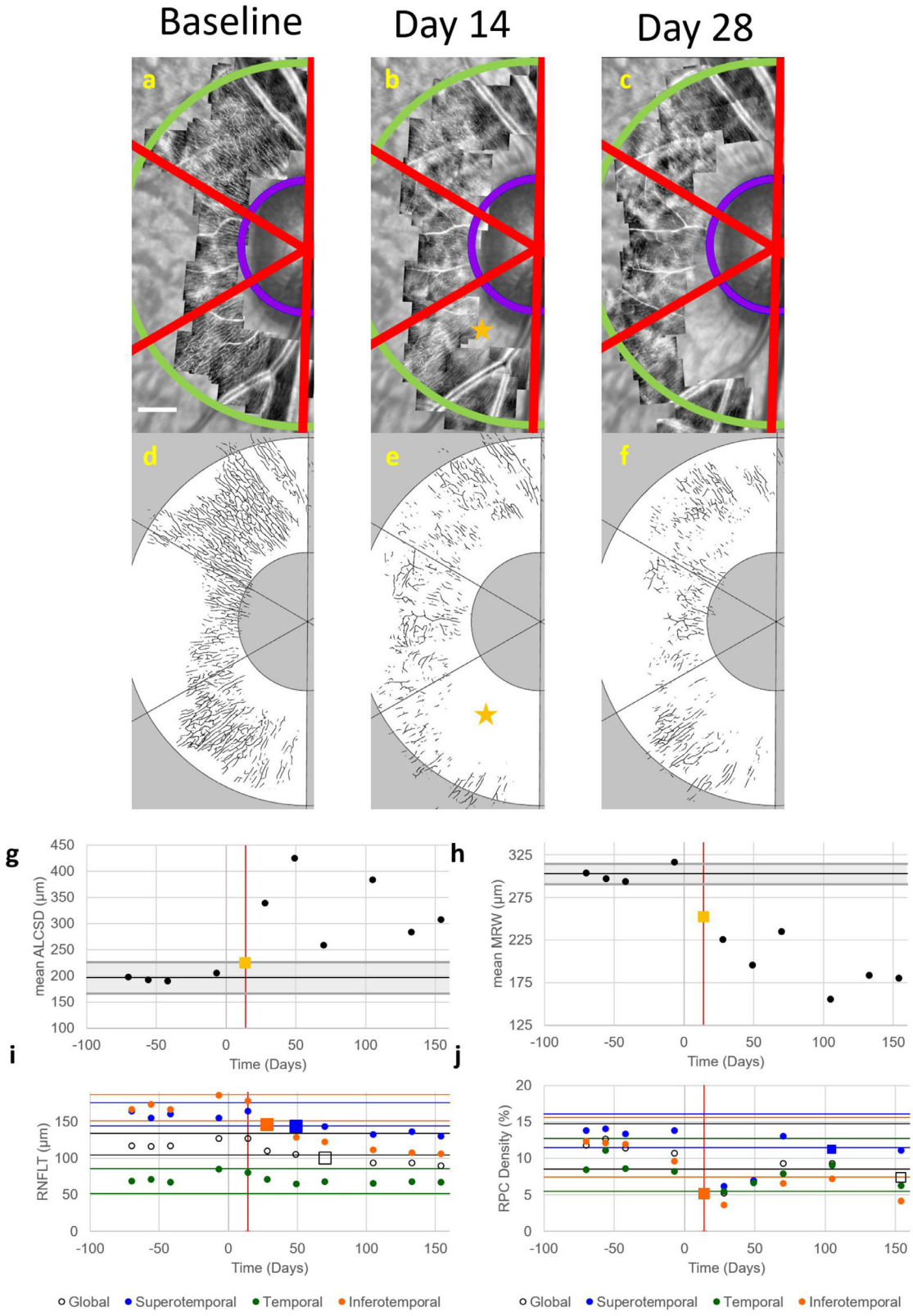

Figure 4. RPC perfusion density changed prior to an initial change in RNFL thickness in the EG eye of OHT-81. Images of **(a–c)** perfused RPCs and **(d–f)** their corresponding automatic segmentations acquired in the EG eye of OHT-81 at baseline (*left column*), the timepoint corresponding to the first significant change in RPC perfusion density (*middle column*, 14 days after the initial laser session), and the timepoint of first significant change in RNFL thickness (*right column*, 28 days after the initial laser session). (Note: Not all imaging timepoints are included in this figure.) Perfused RPC density was analyzed globally and in 60° sectors (*red boundary lines*) within the annulus between 3° (*inner purple arc*) and 8° (*outer green arc*) from the center of the BMO ellipse. *Scale bar* in **a:** 400 µm. The first significant change in RPC perfusion density was measured in the inferotemporal sector at 14 days after the first laser session (*yellow star*). Values for **(g)** mean ALCSD

and **(h)** mean MRW are plotted as a function of time for all imaging timepoints before and after the time of the initial laser session (day 0). *Black horizontal lines* represent the mean baseline value for these two parameters. *Gray shaded regions* represent the 95% confidence interval for each parameter calculated from data measured in the fellow control eye, with *yellow squares* representing the time of first significant change. Values of **(i)** RNFLT and **(j)** RPC density are plotted for global measures (*black open circle*) and for superotemporal (*blue circle*), temporal (*green circle*), and inferotemporal (*orange circle*) sectors at the same imaging timepoints. Corresponding colored horizontal lines indicate the 95% confidence interval for each measure, with *square markers* representing the time of first significant change. *Vertical red lines* in all plots indicate the first timepoint of significant change in RPC perfusion density. The first parameters to change in OHT-81 were **(g)** mean ALCSD, **(h)** mean MRW, and **(j)** RPC density in the inferotemporal sector at day 14. RNFL thickness changed first in the inferotemporal sector at day 28.

one, in which RPC density was the first parameter to change.

The in vivo IOP and ONH measurements found in healthy control and EG eyes in this study are similar to values published from other studies. The average maximum IOP measured across all EG eyes in this study was 43.4 ± 10.5 mm Hg, which was 231% greater than the average maximum IOP across the contralateral control eyes of 18.8 ± 2.4 mm Hg. Work from previous studies using the same or a similar method of inducing glaucoma experimentally in NHPs have resulted in a +282%,[35] +280%,[47] and +241%[48] difference in the mean maximum IOP between EG and control eyes. For ONH measures, the average mean ALCSD for all control eyes across all timepoints in this study was 200.7 ± 24.3 µm, which is similar to values of mean ALSCD reported previously in healthy NHP eyes (ranging from 214–230 µm).[35,49–51] The average mean MRW for all control eyes across all timepoints in this study (340.0 ± 50.7 µm) is also similar to the mean value previously reported in control eyes by Ivers et al.[35] (308.7 ± 55.1 µm) and is within the range reported by Strouthidis et al. (~200 - 425 µm).[49] In addition, the mean global RNFLT measured in the control eyes over the course of this study (116.4 ± 6.8 µm) is within the range of values of global RNFLT published in healthy NHP eyes (~101 – 124 µm).[35,39,52,53]

Coefficients of repeatability (CRs) computed using the control eye data for all OCT-derived parameters in this study were also consistent with CRs for the same metrics reported by other studies. The CRs for mean ALCSD (20.8 µm ± 6.4 µm), mean MRW (16.9 µm ± 5.9 µm), and global RNFLT (6.1 µm ± 1.6 µm) in this study are consistent with previously reported CRs for mean ALCSD (27.1 µm ± 11.9 µm),[35] mean MRW (20.0 µm and 20.6 µm),[35,39] and global RNFLT (4.9 µm and 5.5 µm).[35,39] The low CRs found in this study for the OCT-derived metrics and their similarity to values acquired in other studies lend support to the consistency of the experimental methods implemented in this study.

This study reports the first values of RPC perfusion density near the ONH in healthy and diseased NHP eyes based on split detector AOSLO images. AOSLO-based measures of RPC perfusion density acquired in healthy NHP retinas in this study (13.15% ± 2.97%) are lower than OCTA-based measurements of vessel density reported in the NHP eye (35.4% ± 3.4%).[54] One reason for this difference is that only capillaries were included in our calculation of perfusion density, as our primary focus was to determine changes in the RPCs during experimental glaucoma. Hence, we refer to density as *RPC perfusion* density instead of *vessel* density (as traditionally done with OCTA). Inclusion of larger vessels would have increased our AOSLO image-derived density measurements. In addition, because of their correction of the eye's higher order aberrations, AOSLO images have better lateral resolution than OCTA images and have been shown to closely agree with histological images of retinal vasculature.[55] The decreased lateral resolution inherent in OCTA perfusion images yields a broader point (or line) spread function and larger diameter vessels, which can lead to the calculation of higher perfusion densities. Moreover, an OCTA image typically represents a maximum intensity projection that includes vasculature being perfused at multiple depths within the slab being quantified, whereas AOSLO imaging typically collects light over a smaller depth. Consequently, it is likely that less perfused vasculature will be observed in an AOSLO perfusion image over a comparably sized area (relative to an OCTA perfusion image) and yield decreased perfusion density values near the ONH. However, the application of some methods (such as skeletonization) to OCTA images may improve vessel density measurements, potentially bringing them into better agreement with those calculated using histology and adaptive optics.[56]

The CRs for RPC perfusion density as measured near the ONH from images obtained in healthy NHP eyes using split detector AOSLO imaging ranged from 2.3% to 4.1% (or 21.0% to 26.5% of the mean density) across sectors. Coefficients of repeatability were calculated differently for SDOCT-derived metrics (mean ALCSD, mean MRW, RNFLT) and AOSLO-derived RPC density values because the imaging protocol and the time with which animals could remain safely anesthetized led to differences in the number of sessions in which control eye data could be obtained using each modality. Because SDOCT imaging was performed first within an imaging session, ONH scans could be acquired in the control and EG eyes at each experimental timepoint. However, it was not possible to acquire RPC perfusion images in the control eye at all time points as AOSLO imaging, which was performed last and requires a much longer amount of time (relative to SDOCT), was always done first in the EG eye and then in the control eye, if time remained. Given that we were unable to consistently image all sectors in the control eyes at each time point (unlike with SDOCT), we used a different method to determine the CR for RPC perfusion density. Even though different methods were used depending on the imaging modality, we note that the same method was applied across all animals throughout the entire experiment to minimize any potentially deleterious impacts of using a different approach.

Several factors could have contributed to the variability of our RPC density measurements. First, slightly different portions of the retina were imaged within each eye over time despite our best attempts to image the same retinal area. Many AOSLO systems do not have active eye tracking systems, as is common on most SDOCT systems, which makes it more challenging to consistently image the same retinal locations between sessions and likely impacts the variability. Second, there were differences in the percentage of the total area that was covered over time. Our decision to analyze only sectors in which the area imaged with

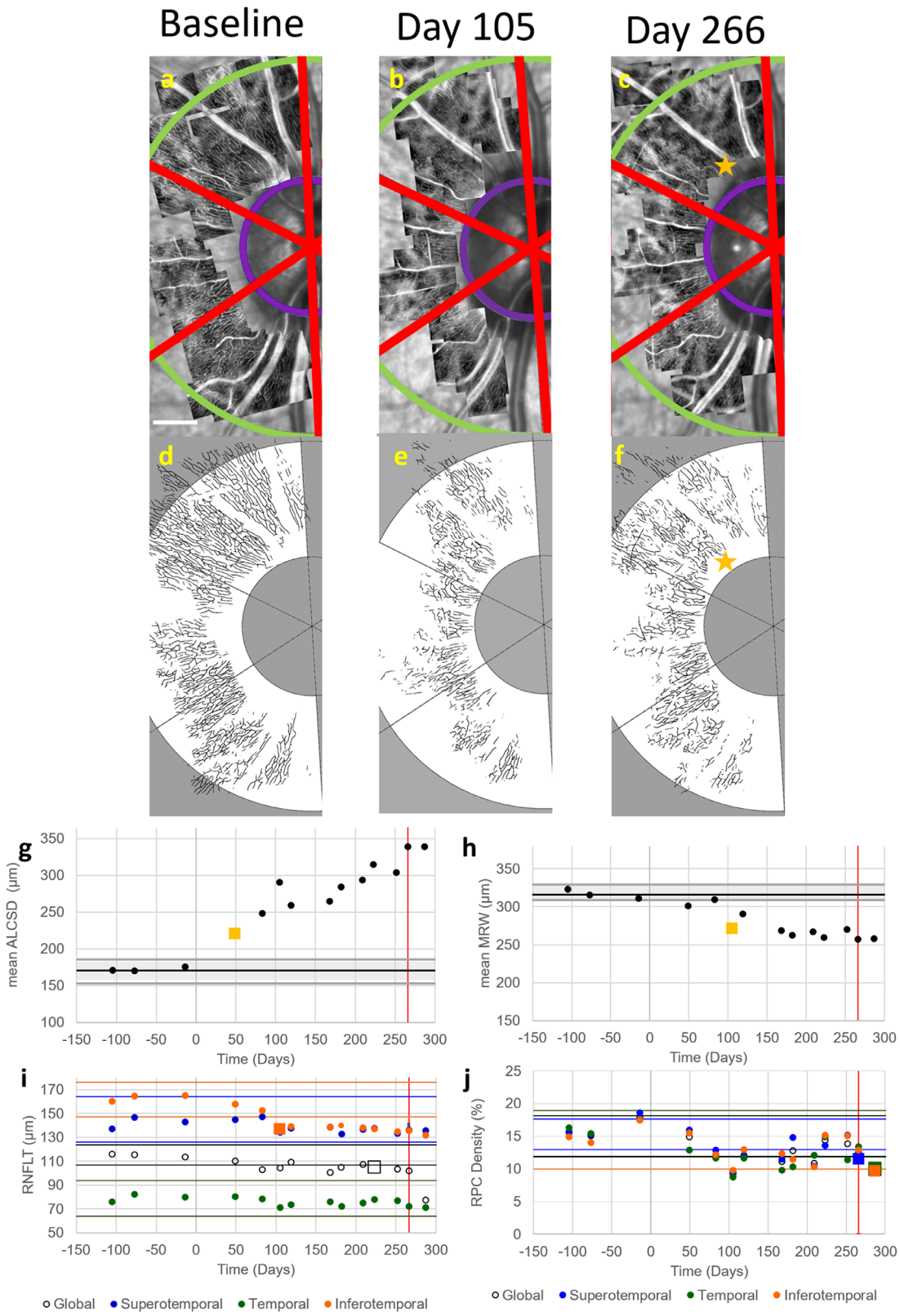

Figure 5. RPC perfusion density changed after the timepoint of first change in RNFL thickness in the EG eye of OHT-79. Images of **(a–c)** perfused RPCs and **(d–f)** their corresponding automatic segmentations acquired in the EG eye of OHT-79 at baseline (*left column*), the timepoint of first significant change in RNFL thickness (*middle column*, 105 days after the initial laser session), and the timepoint of first significant change in RPC perfusion density (*right column*, 266 days after the initial laser session). (Note: Not all imaging timepoints are included in this figure.) Perfused RPC density was analyzed globally and in 60° sectors (*red boundary lines*) within the annulus between 3° (*inner purple arc*) and 8° (*outer green arc*) from the center of the BMO ellipse. *Scale bar* in **a**: 400 µm. The first significant change in RPC perfusion density was measured in the superotemporal sector at 266 days after the initial laser session (*yellow star*). Values for **(g)** mean ALCSD and **(h)** mean MRW are plotted as a function of time for all imaging timepoints before and after the time of the initial laser session (day

0). *Black horizontal lines* represent the mean baseline value for these two parameters. *Gray shaded regions* represent the 95% confidence interval for each parameter calculated from data measured in the fellow control eye, with yellow squares representing the time of first significant change. Values of **(i)** RNFLT and **(j)** RPC density are plotted for global measures (*black open circle*) and for superotemporal (*blue circle*), temporal (*green circle*), and inferotemporal (*orange circle*) sectors at the same imaging timepoints. Corresponding colored horizontal lines indicate the 95% confidence interval for each measure, with *square markers* representing the time of first significant change. *Vertical red lines* in all plots indicate the first timepoint of significant change in RPC perfusion density. The first parameter to change in OHT-79 was **(g)** mean ALCSD (day 49), followed by **(h)** mean MRW (day 105). The next parameter to change was **(i)** RNFLT in the inferotemporal sector (*orange square*, day 105), followed by the last parameter to change, **(j)** RPC perfusion density in the inferotemporal sector (day 266).

the AOSLO exceeded 30% of the total area was based on a trade-off between the amount of coverage we could consistently achieve in all sectors across all imaging timepoints and the number of timepoints that this threshold allowed us to quantify RPC perfusion density for each sector. It is possible that the CR could have been lower if this threshold was higher. Third, the repeatability could have been impacted by fluctuations in image specific parameters. For example, AOSLO image quality is sometimes not uniform throughout the experiment. Consistent with studies that have reported alterations in axonal reflectivity and birefringence with experimental glaucoma,[57,58] the reflectivity of axon bundles in confocal AOSLO images can decrease with progression and make it more challenging to visualize the intertwining RPCs from split detector images. Also, for each AOSLO imaging session, the plane of best focus for imaging the RPCs is manually selected after using the confocal AOSLO channel to section through the retina and visualize the most superficial retinal nerve fiber bundles. Since the retina is a curved surface and retinal thickness is uneven around the ONH, the focus must be checked throughout the imaging session as the imaged location changes. Automating the focus selection and adding eye tracking capabilities to the AOSLO system could potentially decrease variability in the areas imaged between sessions and result in smaller confidence intervals for RPC perfusion density. An additional factor that could impact the CR is the size of the field of view of the image. Lee et al.[59] evaluated the coefficient of variability (CoV) for macular vessel density using OCTA images of different field sizes and found that the CoV for vessel density was much greater when using a small, 1 mm × 1 mm scan (18.552%) compared to a larger, 6 mm × 6 mm scan (4.042%). The smaller field size of the individually acquired AOSLO images (~0.6 mm × 0.6 mm field of view) could contribute to a larger CR. Finally, quantification of the RPC density depends on the method used to covert the grayscale AOSLO images to binary images. The automated segmentation algorithm used for this dataset, which was trained on RPC images of varying image quality from healthy human and NHP eyes, and eyes from NHPs with EG, was shown to be 94% accurate when compared to markings made by manual graders. Although quantification of perfused vasculature could have been improved with manual correction of the automatic segmentation, such a process would have been very time inefficient and would have increased the subjectivity of our approach. Despite these challenges and the variability reported, vascular changes were still noted before changes in RNFLT in several EG eyes in this study.

Mean ALCSD and/or mean MRW were the first measured parameters to change in eight of nine animals, whereas no NHPs had significant RNFL thinning prior to a change in any ONH parameter. These findings are consistent with other studies that have examined ONH parameters and RNFLT and found that ONH-related parameters tend to change before retinal parameters.[35,49] An initial change in RPC perfusion density occurred simultaneous with an initial change in an ONH parameter in two of the eight aforementioned eyes, while also occurring solely on its own in the ninth eye (i.e., in OHT 86, before a measured change in any ONH parameter in that eye). The first change in RPC perfusion density was measured simultaneous to or after a first change in an ONH parameter in eight of nine EG eyes. Future experiments could examine the extent to which a loss in RPC perfusion is a more primary mechanism of glaucoma in some eyes or possibly occurs secondarily as a consequence of ONH changes in other eyes.

Decreases in RPC perfusion could potentially decrease the supply of nutrients to and the removal of waste from RNFL axons in the region of perfusion loss. Therefore a local loss in RPC perfusion could be expected to result in a subsequent loss in RNFL axons (or a decrease in RNFLT) in the corresponding local area. Such local relationships were observed in some EG eyes in this study. For example, an initial loss in RPC perfusion density in the inferotemporal sector was observed within the EG eye of OHT 81 (Fig. 4j, day 14) before an initial thinning of the RNFL in the corresponding inferotemporal sector (Fig. 4i, day 28). Similarly, RPC perfusion density decreased in the superotemporal sector within the EG eye of OHT 86 at 70 days after the initial laser session, which was before the first significant decrease measured in RNFLT in the corresponding superotemporal sector at 105 days after the initial laser session (data not shown). In these examples, the time course of alterations in RPC perfusion density and RNFLT may indicate that a loss of perfusion resulted in subsequent damage to RNFL axons in corresponding locations and an ultimate decrease in RNFLT. However, mixed results were found in other EG eyes. For example, while initial decreases in RPC perfusion density were measured in the superotemporal and temporal sectors of OHT 82 (Fig. 6h, day 133) before an initial thinning of the RNFL in the corresponding superotemporal and temporal sectors (Fig. 6g, day 182), an opposite relationship was found in the inferotemporal sector of the same eye, in which RNFLT decreased (day 133) before an initial decrease in RPC perfusion density (day 182). In another example, RPC perfusion density first decreased in the temporal sector within the EG eye of OHT 78 at 83 days after the initial laser session (data not shown) whereas a change in RNFLT relative to baseline was never measured in the corresponding temporal sector.

Different reasons could account for the different patterns of loss in RPC perfusion density and RNFLT in the EG eyes examined in this study. First, it is quite possible that RNFL axons have different susceptibilities to changes in vascular perfusion in different eyes. Second, despite our best efforts to consistently image the same retinal regions, it is also possible that alterations in RPC perfusion occurred outside of the regions that were imaged at a given timepoint or outside of the annulus analyzed in this work. Furthermore, these observed patterns were influenced by our method for

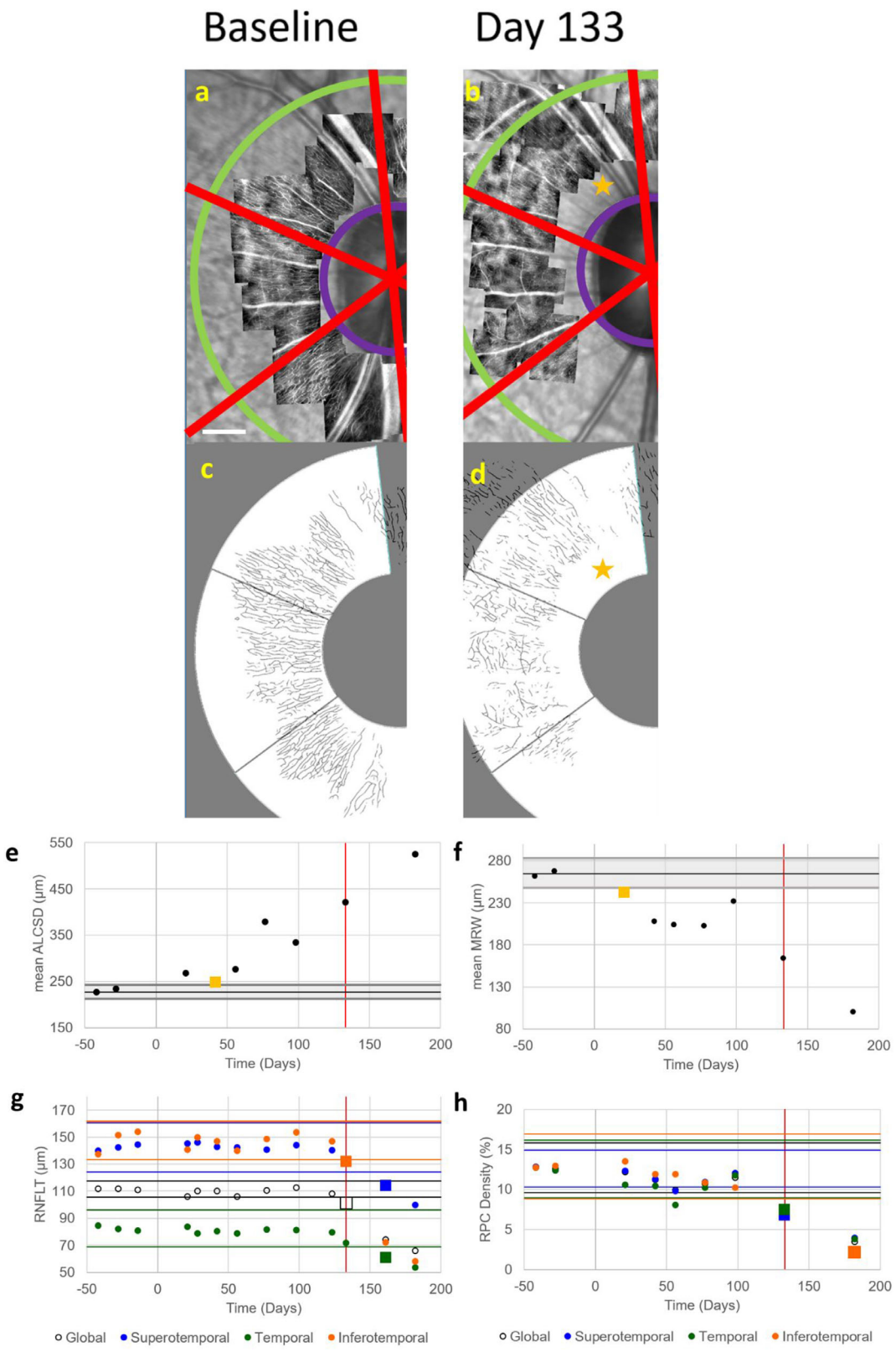

Figure 6. Initial changes in RPC perfusion density and RNFL thickness occurred simultaneously in the EG eye of OHT-82. Images of **(a, b)** perfused RPCs and **(c, d)** their corresponding automatic segmentations acquired in the EG eye of OHT-82 at baseline (*left column*) and the timepoint corresponding to the first significant changes in RPC perfusion density and RNFL thickness (*right column*, 133 days after the initial laser session). (Note: Not all imaging timepoints are included in this figure.) Perfused RPC density was analyzed globally and in 60° sectors (*red boundary lines*) within the annulus between 3° (*inner purple arc*) and 8° (*outer green arc*) from the center of the BMO ellipse. *Scale bar* in **a:** 400 µm. The first significant change in RPC perfusion density was measured in the superotemporal sector at 133 days after the initial-laser session (*yellow star*). Values for **(e)** mean ALCSD and **(f)** mean MRW are plotted as a function of time for all imaging timepoints before and after the time of the initial laser session (day 0). *Black horizontal lines* represent the mean baseline value for these

two parameters. *Gray shaded regions* represent the 95% confidence interval for each parameter calculated from data measured in the fellow control eye, with *yellow squares* representing the time of first significant change. Values of (g) RNFLT and (h) RPC density are plotted for global measures (*black open circle*) and for superotemporal (*blue circle*), temporal (*green circle*), and inferotemporal (*orange circle*) sectors at the same imaging timepoints. Corresponding colored horizontal lines indicate the 95% confidence interval for each measure, with *square markers* representing the time of first significant change. *Vertical red lines* in all plots indicate the first timepoint of significant change in RPC perfusion density. The first parameter to change in OHT-82 was **(f)** mean MRW (day 21), followed by **(e)** mean ALCSD (day 42). Initial decreases in global and sectoral values of RPC perfusion density and RNFLT occurred simultaneously at day 133.

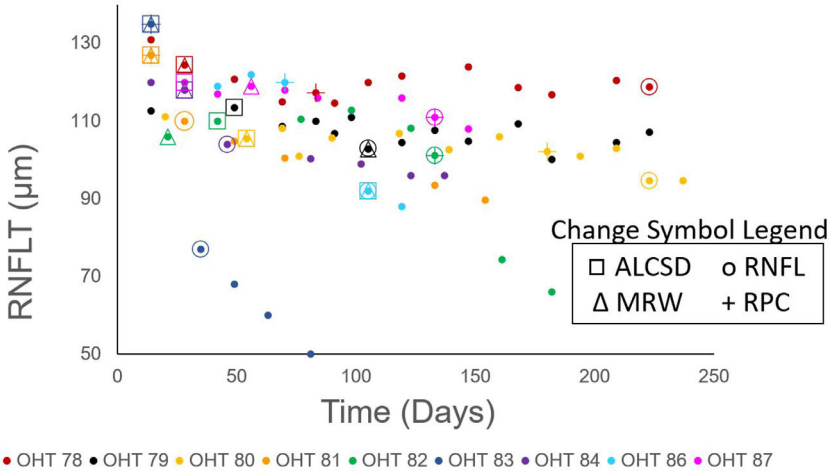

Figure 7. Time of first significant change measured in all parameters for each EG eye. RNFLT values are plotted as a function of study time for all EG eyes (*filled circles*, with each color representing a different EG eye). The timepoints corresponding to the first significant change in mean ALCSD, mean MRW, RNFLT, and RPC density on a global or sectoral level are shown using a *square*, *triangle*, *circle*, and *cross*, respectively. A progressive decrease in global RNFLT was measured throughout the course of the study for all EG eyes. An increase in mean ALCSD (*square*) was the first structural change to occur in 7 of 9 EG eyes. A change in mean MRW (*triangle*) and RPC perfusion density (*cross*) simultaneously accompanied this first change in 6 EG eyes and 2 EG eyes, respectively. A decrease in RPC perfusion density was the first structural change to solely occur in one EG eye (OHT 86). The first change in RPC perfusion density occurred before the first change in RNFLT (*circle*) in 5 of 9 EG eyes.

determining the timepoint of first change (i.e., the time when a given parameter first fell outside of its confidence interval limits *and* remained outside of these limits). While the focus of this study was on early experimental glaucoma, it could have been possible for an ONH or retinal parameter to have rebounded back within the confidence interval in an EG eye if each experiment continued fully to "end stage." We believe the likelihood for this occurrence is low for the vast majority of eyes as 7 of 9 EG eyes experienced significant neuropathy (i.e., had a mean percentage loss of RNFLT between 13% and 62%) by the end of the experiment. In addition, with the exception of one animal that was followed for 14 days after the first change in RPC density (OHT-87), all other animals were followed for anywhere from 49 to 295 days after the first change in RPC density, and no rebound was observed. In addition, different results could have been found if we only considered the timepoint at which a given parameter first fell outside of the confidence interval and did not require that the parameter remain outside of the interval. For example, RPC perfusion density measured in the superotemporal sector within OHT 81 (Fig. 4j) first fell outside of its confidence interval at day 14, but rebounded back within the confidence interval at a later timepoint (day 70) before dropping back outside and remaining outside of the confidence interval at day 105. Due to our more conservative criterion (i.e., requiring the parameter to also remain outside of the confidence interval), the reported time of the first change was 105 days. However, without this criterion, the initial change would have occurred at day 14, which would have been before the first measured change in RNFLT in the superotemporal sector (Fig. 4i) at day 49. The rebound in mean ALCSD, mean MRW, and RPC perfusion density observed in the superotemporal sector of the EG eye at day 70 could likely have been due to a lower pre-imaging session IOP (18 mm Hg) at this time point relative to the previous session (38 mm Hg), possibly resulting in an associated hysteresis in structural measures. In addition, it could be plausible that the capillaries imaged at later timepoints contained both RPCs and deeper capillaries that were subsequently visible due to losses in overlying RPCs. Although great effort was taken to ensure that only the most superficial capillaries were imaged at each timepoint, it is possible that the most superficial capillary network that was visible at later timepoints in an EG eye with a reduced RNFL could have been a deeper capillary plexus. Also, it is important to recall that perfusion images only show vessels that are actively perfused. If capillaries are nonperfused because of an ischemic event or blockage upstream of the capillary blood supply that later resolves, capillaries could reperfuse and be imaged at a later time.[60] Decreased autoregulation of the capillary network could also result in transient perfusion decreases. It has been shown (using Doppler laser flowmetry) that there is decreased autoregulation of blood flow in the major vasculature in the ONH in eyes with glaucoma.[61] Some eyes could be more susceptible to decreased vascular autoregulation and vascular instabilities could be more prominent in these eyes, leading to alterations in perfusion over time. In particular, patients with normal tension glau-

coma could have more perfusion alterations as many vascular risk factors have been associated with normal tension glaucoma.[5,6,9,10,62,63] It is important to note that a pressure-based model of experimental glaucoma was used in this study. Although we know of no non-human primate models of normal tension glaucoma, further research could examine RPC perfusion over time in human patients with normal-tension glaucoma.

In summary, we longitudinally examined the time course of earliest change in radial peripapillary capillaries in a monkey model of experimental glaucoma. The results from this study show that RPCs change prior to a decrease in RNFLT in the majority of eyes with experimental glaucoma. These data suggest that vascular factors may make some eyes more susceptible to axonal loss in early stages of the disease. Future work could examine changes in RPC perfusion and structure in tandem with assessments of blood pressure, intracranial pressure and ocular perfusion pressure to better understand vascular dynamics and their implications in the development and progression of glaucoma.

Acknowledgments

The authors thank Ron Harwerth for helpful discussions and guidance during the NHP experiments. The authors acknowledge the use of the Maxwell/Opuntia/Sabine Clusters and the advanced support from the Research Computing Data Core at the University of Houston.

Supported by BrightFocus Foundation National Glaucoma Research Grant (G2018061), NIH Grants R01 EY029229 and P30 EY007551, and the University of Houston College of Optometry.

Disclosure: **G. Musial,** None; **S. Adhikari,** None; **H. Mirhajianmoghadam,** None; **H.M. Queener,** None; **A.W. Schill,** None; **N.B. Patel,** None; **J. Porter,** None

References

1. Quigley H, Broman AT. The number of people with glaucoma worldwide in 2010 and 2020. *Br J Ophthalmol*. 2006;90:262–267.
2. Bonomi L, Marchini G, Marraffa M, Bernardi P, Morbio R, Varotto A. Vascular risk factors for primary open angle glaucoma: the Egna-Neumarkt Study. *Ophthalmology*. 2000;107:1287–1293.
3. Flower R, Peiretti E, Magnani M, et al. Observation of erythrocyte dynamics in the retinal capillaries and choriocapillaris using ICG-loaded erythrocyte ghost cells. *Investig Ophthalmol Vis Sci*. 2008;49:5510–5516.
4. Grzybowski A, Och M, Kanclerz P, Leffler C, De Moraes CG. Primary open angle glaucoma and vascular risk factors: a review of population based studies from 1990 to 2019. *J Clin Med*. 2020;9:761.
5. Xu C, Li J, Li Z, Mao X. Migraine as a risk factor for primary open angle glaucoma: A systematic review and meta-analysis. *Medicine (Baltimore)*. 2018;97(28):e11377.
6. Wang Jie Jin, Mitchell P, Smith W. Is there an association between migraine headache and open-angle glaucoma? Findings from the Blue Mountains Eye Study. *Ophthalmology*. 1997;104:1714–1719.
7. Park HYL, Park SH, Oh YS, Park CK. Nail bed hemorrhage: a clinical marker of optic disc hemorrhage in patients with glaucoma. *Arch Ophthalmol*. 2011;129:1299–1304.
8. Yanagi M, Kawasaki R, Wang JJ, Wong TY, Crowston J, Kiuchi Y. Vascular risk factors in glaucoma: a review. *Clin Experiment Ophthalmol*. 2011;39:252–258.
9. Binggeli T, Schoetzau A, Konieczka K. In glaucoma patients, low blood pressure is accompanied by vascular dysregulation. *EPMA J*. 2018;9:387–391.
10. Kaiser HJ, Flammer J. Systemic hypotension: a risk factor for glaucomatous damage? *Ophthalmologica*. 1991;203:105–108.
11. Agarwal R, Gupta SK, Agarwal P, Saxena R, Agrawal S. Current concepts in the pathophysiology of glaucoma. *Indian J Ophthalmol*. 2009;57:257–266.
12. Wilson MR, Hertzmark E, Walker AM, Childs Shaw K, Epstein DL. A case-control study of risk factors in open angle glaucoma. *Arch Ophthalmol*. 1987;105:1066–1071.
13. Chan KKW, Tang F, Tham CCY, Young AL, Cheung CY. Retinal vasculature in glaucoma: a review. *BMJ Open Ophthalmol*. 2017;1(1):e000032.
14. Fechtner RD, Weinreb RN. Mechanisms of optic nerve damage in primary open angle glaucoma. *Surv Ophthalmol*. 1994;39(1):23–42.
15. Grieshaber MC, Mozaffarieh M, Flammer J. What is the link between vascular dysregulation and glaucoma? *Surv Ophthalmol*. 2007;52(6 Suppl.):144–154.
16. Jonas JB, Wang N. Intracranial pressure and glaucoma. *J Glaucoma*. 2013;22(Suppl 5):S13–S14.
17. Hogan MJ, Alvarado JA, Wedell JE. *Retina. Histology of the human eye: an atlas and textbook*. Philadelphia: Saunders; 1971.
18. Daicker B. Selective atrophy of the radial peripapillary capillaries and visual field defects in glaucoma. *Albrecht Von Graefes Arch Klin Exp Ophthalmol*. 1975;195:27–32.
19. Quigley HA, Hohman RM, Addicks EM, Green WR. Blood vessels of the glaucomatous optic disc in experimental primate and human eyes. *Invest Ophthalmol Vis Sci*. 1984;25:918–931.
20. Quigley HA, Green WR. The histology of human glaucoma cupping and optic nerve damage: clinicopathologic correlation in 21 eyes. *Ophthalmology*. 1979;86:1803–1827.
21. Alterman M, Henkind P. Radial peripapillary capillaries of the retina. II. Possible role in Bjerrum scotoma. *Br J Ophthalmol* 1968;52:26–31.
22. Kornzweig AL, Eliasoph I, Feldstein M. Selective atrophy of the radial peripapillary capillaries in chronic glaucoma. *Arch Ophthalmol*. 1968;80:696–702.
23. Liu L, Jia Y, Takusagawa HL, et al. Optical coherence tomography angiography of the peripapillary retina in glaucoma. *JAMA Ophthalmol*. 2015;133:1045–1052.
24. Akagi T, Iida Y, Nakanishi H, et al. Microvascular density in glaucomatous eyes with hemifield visual field defects: an optical coherence tomography angiography study. *Am J Ophthalmol*. 2016;168:237–249.
25. Mammo Z, Heisler M, Balaratnasingam C, et al. Quantitative optical coherence tomography angiography of radial peripapillary capillaries in glaucoma, glaucoma suspect, and normal eyes. *Am J Ophthalmol*. 2016;170:41–49.
26. Chen CL, Bojikian KD, Wen JC, et al. Peripapillary retinal nerve fiber layer vascular microcirculation in eyes with glaucoma and single-hemifield visual field loss. *JAMA Ophthalmol*. 2017;135:461–468.
27. Yarmohammadi A, Zangwill LM, Diniz-Filho A. Peripapillary and macular vessel density in patients with glaucoma and single-hemifield visual field defect. *Ophthalmology*. 2017;124:709–719.
28. Moghimi S, Zangwill LM, Penteado RC, et al. Macular and optic nerve head vessel density and progressive retinal nerve fiber layer loss in glaucoma. *Ophthalmology*. 2018;125:1720–1728.
29. Yarmohammadi A, Zangwill LM, Diniz-Filho A, et al. Optical coherence tomography angiography vessel density in healthy, glaucoma suspect, and glaucoma eyes. *Invest Ophthalmol Vis Sci*. 2016;57(9):OCT451–OCT459.

30. Sulai YN, Scoles D, Harvey Z, Dubra A. Visualization of retinal vascular structure and perfusion with a nonconfocal adaptive optics scanning light ophthalmoscope. *J Opt Soc Am A*. 2014;31:569.
31. Mirhajianmoghadam H, Jnawali A, Musial G, et al. In vivo assessment of foveal geometry and cone photoreceptor density and spacing in children. *Sci Rep*. 2020;10:1–14.
32. Harwerth RS, Smith EL, DeSantis L. Experimental glaucoma: Perimetric field defects and intraocular pressure. *J Glaucoma*. 1997;6:390–401.
33. Frishman LJ, Shen FF, Du L, et al. The scotopic electroretinogram of macaque after retinal ganglion cell loss from experimental glaucoma. *Invest Ophthalmol Vis Sci*. 1996;37:125–141.
34. Ivers KM, Li C, Patel N, et al. Reproducibility of measuring lamina cribrosa pore geometry in human and nonhuman primates with in vivo adaptive optics imaging. *Invest Ophthalmol Vis Sci*. 2011;52:5473–5480.
35. Ivers KM, Sredar N, Patel NB, et al. In vivo changes in lamina cribrosa microarchitecture and optic nerve head structure in early experimental glaucoma. *PLoS One*. 2015;10(7):e0134223.
36. Sredar N, Ivers KM, Queener HM, Zouridakis G, Porter J. 3D modeling to characterize lamina cribrosa surface and pore geometries using in vivo images from normal and glaucomatous eyes. *Biomed Opt Express*. 2013;4:1153.
37. Chen TC. Spectral domain optical coherence tomography in glaucoma: qualitative and quantitative analysis of the optic nerve head and retinal nerve fiber layer (an AOS thesis). *Trans Am Ophthalmol Soc*. 2009;107:254–281.
38. Reis ASC, Zangalli CeS, Abe RY, et al. Intra- and interobserver reproducibility of Bruch's membrane opening minimum rim width measurements with spectral domain optical coherence tomography. *Acta Ophthalmol*. 2017;95(7):e548–e555.
39. Patel NB, Sullivan-Mee M, Harwerth RS. The relationship between retinal nerve fiber layer thickness and optic nerve head neuroretinal rim tissue in glaucoma. *Invest Ophthalmol Vis Sci*. 2014;55:6802–6816.
40. Yu PK, Balaratnasingam C, Xu J, et al. Label-free density measurements of radial peripapillary capillaries in the human retina. *PLoS One*. 2015;10(8):1–14.
41. Delori FC, Webb RH, Sliney DH. Maximum permissible exposures for ocular safety (ANSI 2000), with emphasis on ophthalmic devices. *J Opt Soc Am A Opt Image Sci Vis*. 2007;24:1250–1265.
42. Scoles D, Sulai YN, Langlo CS, et al. In vivo imaging of human cone photoreceptor inner segments. *Invest Ophthalmol Vis Sci*. 2014;55:4244–4251.
43. Burns SA, Elsner AE, Chui TY, et al. In vivo adaptive optics microvascular imaging in diabetic patients without clinically severe diabetic retinopathy. *Biomed Opt Express*. 2014;5:961–974.
44. Musial G, Queener HM, Adhikari S, et al. Automatic segmentation of retinal capillaries in adaptive optics scanning laser ophthalmoscope perfusion images using a convolutional neural network. *Transl Vis Sci Technol*. 2020;9(2):1–14.
45. Otsu N. A threshold selection method from gray-level histograms. *IEEE Trans Syst Man Cybern*. 1979;20(1):62–66.
46. Chauhan BC, Danthurebandara VM, Sharpe GP, et al. Bruch's membrane opening minimum rim width and retinal nerve fiber layer thickness in a normal white population: a multicenter study. *Ophthalmology*. 2015;122:1786–1794.
47. Fortune B, Burgoyne CF, Cull G, Reynaud J, Wang L. Onset and progression of peripapillary retinal nerve fiber layer (RNFL) retardance changes occur earlier than RNFL thickness changes in experimental glaucoma. *Invest Ophthalmol Vis Sci*. 2013;54:5653–5661.
48. Downs JC, Ensor ME, Bellezza AJ, Thompson HW, Hart RT, Burgoyne CF. Posterior scierai thickness in perfusion-fixed normal and early-glaucoma monkey eyes. *Invest Ophthalmol Vis Sci*. 2001;42:3202–3208.
49. Strouthidis NG, Fortune B, Yang H, Sigal IA, Burgoyne CF. Longitudinal change detected by spectral domain optical coherence tomography in the optic nerve head and peripapillary retina in experimental glaucoma. *Invest Ophthalmol Vis Sci*. 2011;52:1206–1219.
50. Strouthidis NG, Fortune B, Yang H, Sigal IA, Burgoyne CF. Effect of acute intraocular pressure elevation on the monkey optic nerve head as detected by spectral domain optical coherence tomography. *Invest Ophthalmol Vis Sci*. 2011;52:9431–9437.
51. Yang H, Qi J, Hardin C, et al. Spectral-domain optical coherence tomography enhanced depth imaging of the normal and glaucomatous nonhuman primate optic nerve head. *Invest Ophthalmol Vis Sci*. 2012;53:394–405.
52. Fortune B, Yang H, Strouthidis NG, et al. The effect of acute intraocular pressure elevation on peripapillary retinal thickness, retinal nerve fiber layer thickness, and retardance. *Invest Ophthalmol Vis Sci*. 2009;50:4719–4726.
53. Fortune B, Cull G, Reynaud J, Wang L, Burgoyne CF. Relating retinal ganglion cell function and retinal nerve fiber layer (RNFL) retardance to progressive loss of RNFL thickness and optic nerve axons in experimental glaucoma. *Invest Ophthalmol Vis Sci*. 2015;56:3936–3944.
54. Patel N, McAllister F, Pardon L, Harwerth R. The effects of graded intraocular pressure challenge on the optic nerve head. *Exp Eye Res*. 2018;169:79–90.
55. Scoles D, Gray DC, Hunter JJ, et al. In-vivo imaging of retinal nerve fiber layer vasculature: Imaging histology comparison. *BMC Ophthalmol*. 2009;9(1):1–9.
56. Mo S, Krawitz B, Efstathiadis E, et al. Imaging foveal microvasculature: Optical coherence tomography angiography versus adaptive optics scanning light ophthalmoscope fluorescein angiography. *Invest Ophthalmol Vis Sci*. 2016;57(9):OCT130–OCT140.
57. Gardiner SK, Demirel S, Reynaud J, Fortune B. Changes in retinal nerve fiber layer reflectance intensity as a predictor of functional progression in glaucoma. *Invest Ophthalmol Vis Sci*. 2016;57:1221–1227.
58. Fortune B, Cull GA, Burgoyne CF. Relative course of retinal nerve fiber layer birefringence and thickness and retinal function changes after optic nerve transection. *Invest Ophthalmol Vis Sci*. 2008;49:4444–4452.
59. Lee TH, Bin Lim H, Nam KY, Kim K, Kim JY. Factors affecting repeatability of assessment of the retinal microvasculature using optical coherence tomography angiography in healthy subjects. *Sci Rep*. 2019;9:1–8.
60. Burns SA, Elsner AE, Sapoznik KA, Warner RL, Gast TJ. Adaptive optics imaging of the human retina. *Prog Retin Eye Res*. 2019;68(August 2018):1–30.
61. Wang L, Cull G, Burgoyne CF, Thompson S, Fortune B. Longitudinal alterations in the dynamic autoregulation of optic nerve head blood flow revealed in experimental glaucoma. *Invest Ophthalmol Vis Sci*. 2014;55:3509–3516.
62. Meyer JH, Brandi-Dohrn J, Funk J. Twenty four hour blood pressure monitoring in normal tension glaucoma. *Br J Ophthalmol*. 1996;80:864.
63. Mroczkowska S, Benavente-Perez A, Negi A, Sung V, Patel SR, Gherghel D. Primary open-angle glaucoma vs normal-tension glaucoma: the vascular perspective. *JAMA Ophthalmol*. 2013;131:36–43.

Investigative Ophthalmology & Visual Science